SUPPLEMENTARY FIGURES AND TABLES

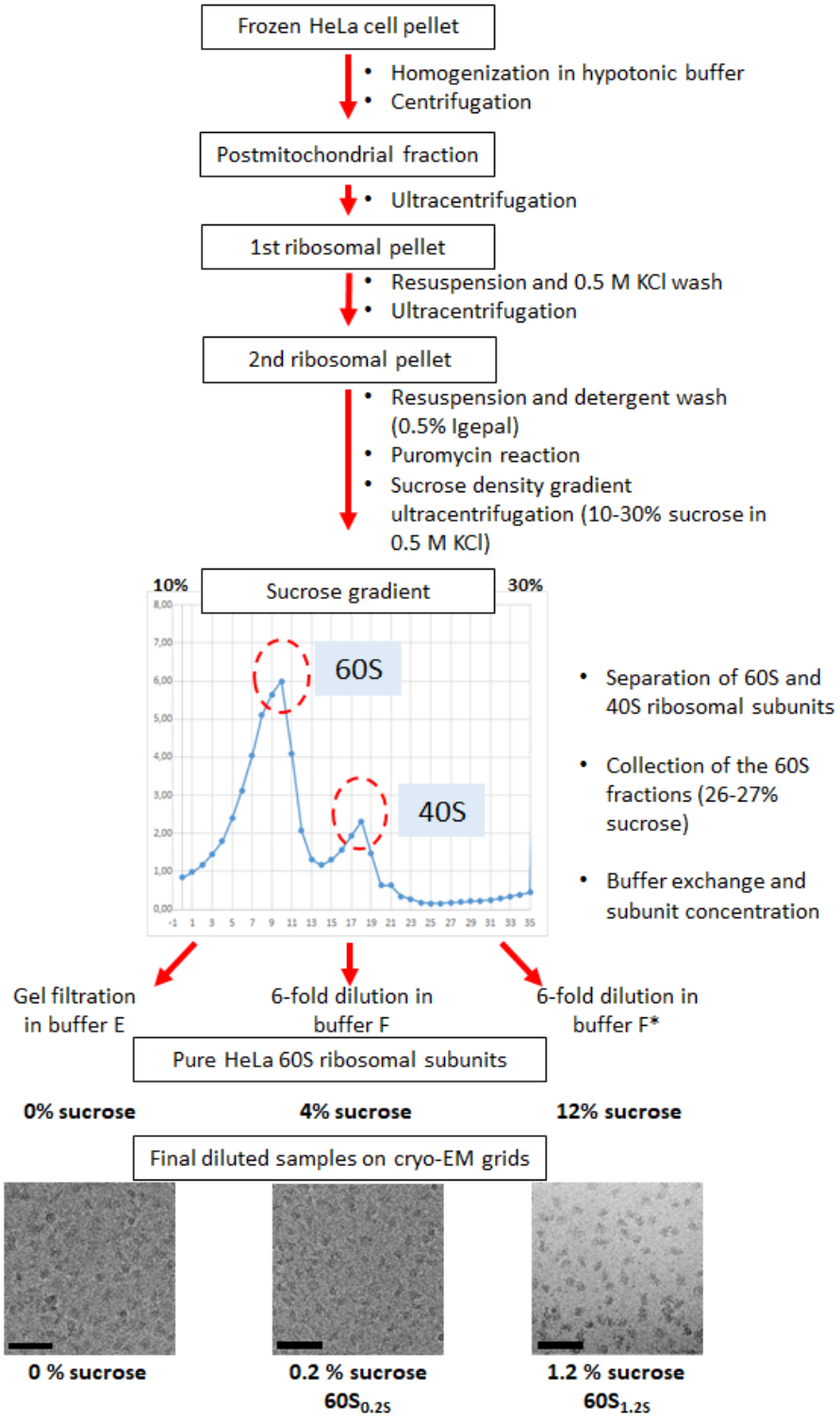

Supplementary Figure 1: Workflow of the 60S ribosomal subunit purification and grid preparation. 60S ribosomal subunits were prepared from frozen HeLa cell pellets using centrifugation and ultracentrifugation steps followed by separation via a sucrose density gradient. The purified subunits were stored in three different buffer conditions containing sucrose in concentrations ranging from 0% to 12%. Prior to grid preparation, the samples were diluted in sucrose-free buffers. Resulting electron micrographs show various degrees of aggregation depending on sucrose concentration in the samples. The defocus values for the EM micrographs are in the range of -2 µm. Scale bars represent 100 nm.

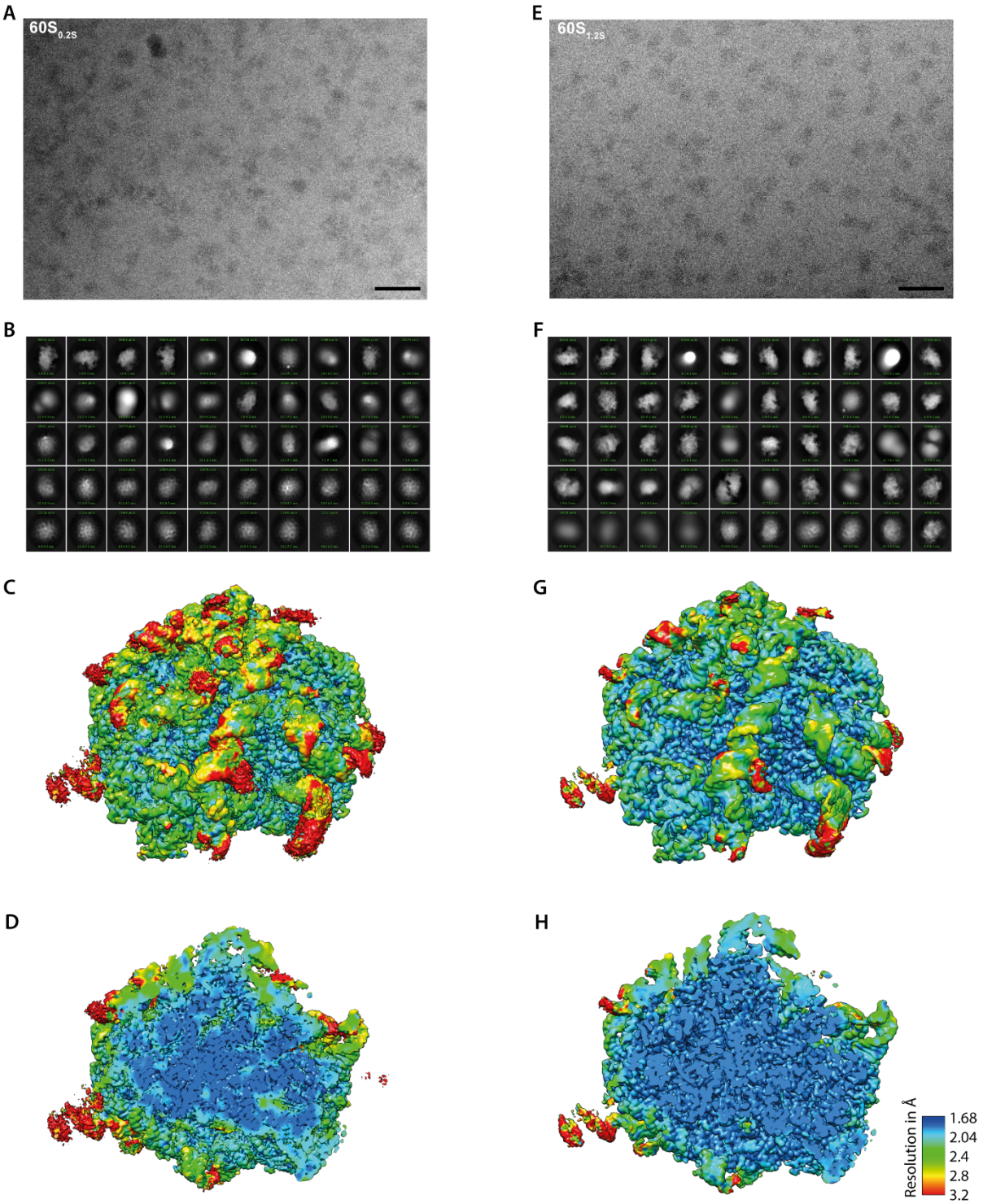

Supplementary Figure 2: Sucrose concentration in the sample influences 60S ribosomal subunit integrity. Comparison of cryo-EM datasets and single-particle 3D reconstructions of HeLa 60S ribosomal subunits vitrified in the presence of 0.2% sucrose **(A-D)** and 1.2% sucrose **(E-H)**. The data sets underwent identical processing and analysis, both resulting in maps with a global resolution of 2.04 Å ($FSC_{0.143}$). **(A,E)** Representative micrographs taken at -1.8 µm defocus showing 60S ribosomal subunit particles. Scale bars represent 50 nm. **(B,F)** 2D class averages from all picked particles classified in 50 classes. $60S_{0.2S}$ particles classified into five "shiny" classes with 22.5% of the particles accumulating to these. In comparison, $60S_{1.2S}$

particles yielded 39 “shiny” classes encompassing 70.2% of the picked particles. **(C,G)** Local resolution maps in crown view with focus on expansion segments. **(D,H)** Central slice through maps in **(C)** and **(G)**. The threshold of the maps was adjusted to show a comparable level of volume in both datasets. The local resolution is color-coded from high resolution in blue (Nyquist-limit 1.648 Å) to lower resolution red (3.2 Å).

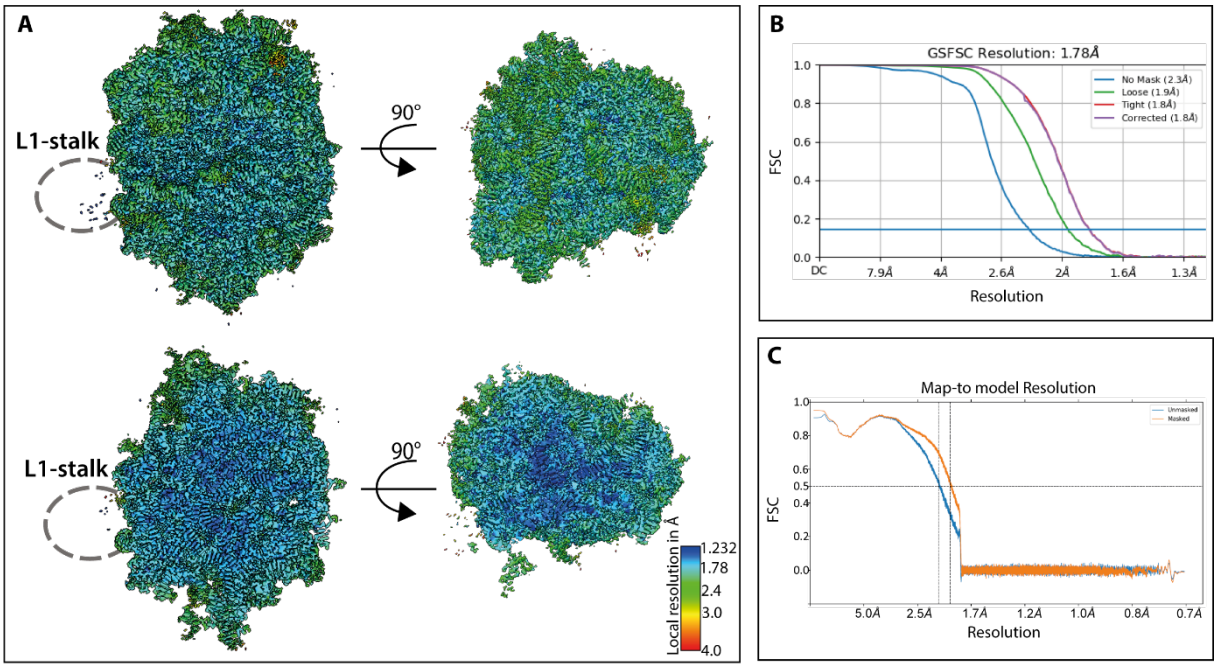

Supplementary Figure 3: Resolution estimation of the 60S ribosomal subunit single-particle reconstruction. **(A)** Local resolution maps of the $60S_{1.2S}$ 3D reconstruction. Top panel: View on the 40S interface of the 60S subunit (left) and the crown-view (right). Bottom panel: Central slice through the map with the same views as above. The resolution limits are color-coded from high resolution in blue (Nyquist-limit 1.236 Å) to lower resolution in red (4.0 Å). **(B)** Fourier shell correlation (FSC) curves from the final refinement in CryoSPARC (1) indicating a global resolution of 1.78 Å ($FSC_{0.143}$) for the $60S_{1.2S}$ 3D reconstruction. **(C)** Map vs. model cross-correlation FSC curves from validation in phenix.validation_cryoem (2) indicating a resolution of 1.87 Å ($FSC_{0.5}$).

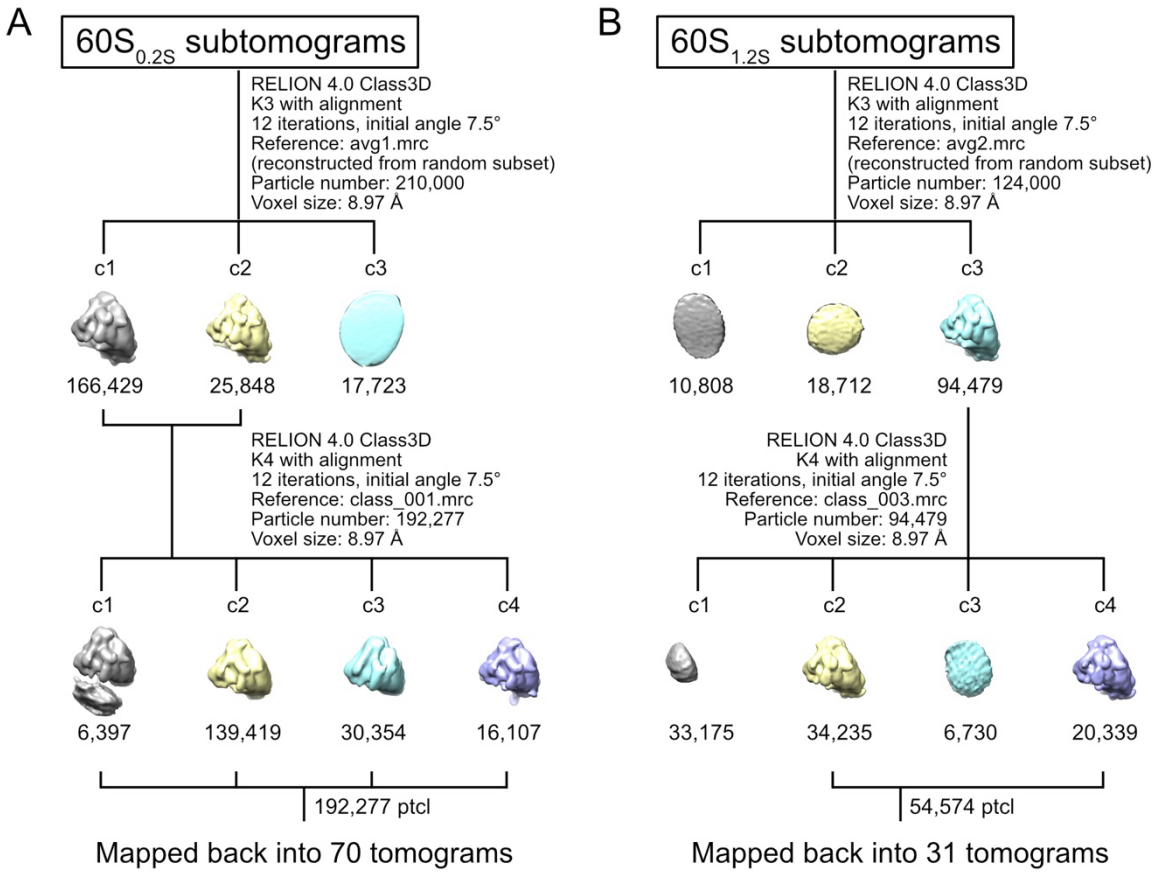

Supplementary Figure 4: Sorting scheme of 60S ribosomal subunit subtomograms. After template matching in Warp (3), subtomograms of $60S_{0.2S}$ **(A)** and $60S_{1.2S}$ **(B)** were extracted at 8.97 Å voxel size (bin 4) and classified in 3D using RELION 4.0 (4), to remove false positive picks. The final particle coordinates were mapped back into the tomograms (Supplementary Figure 5).

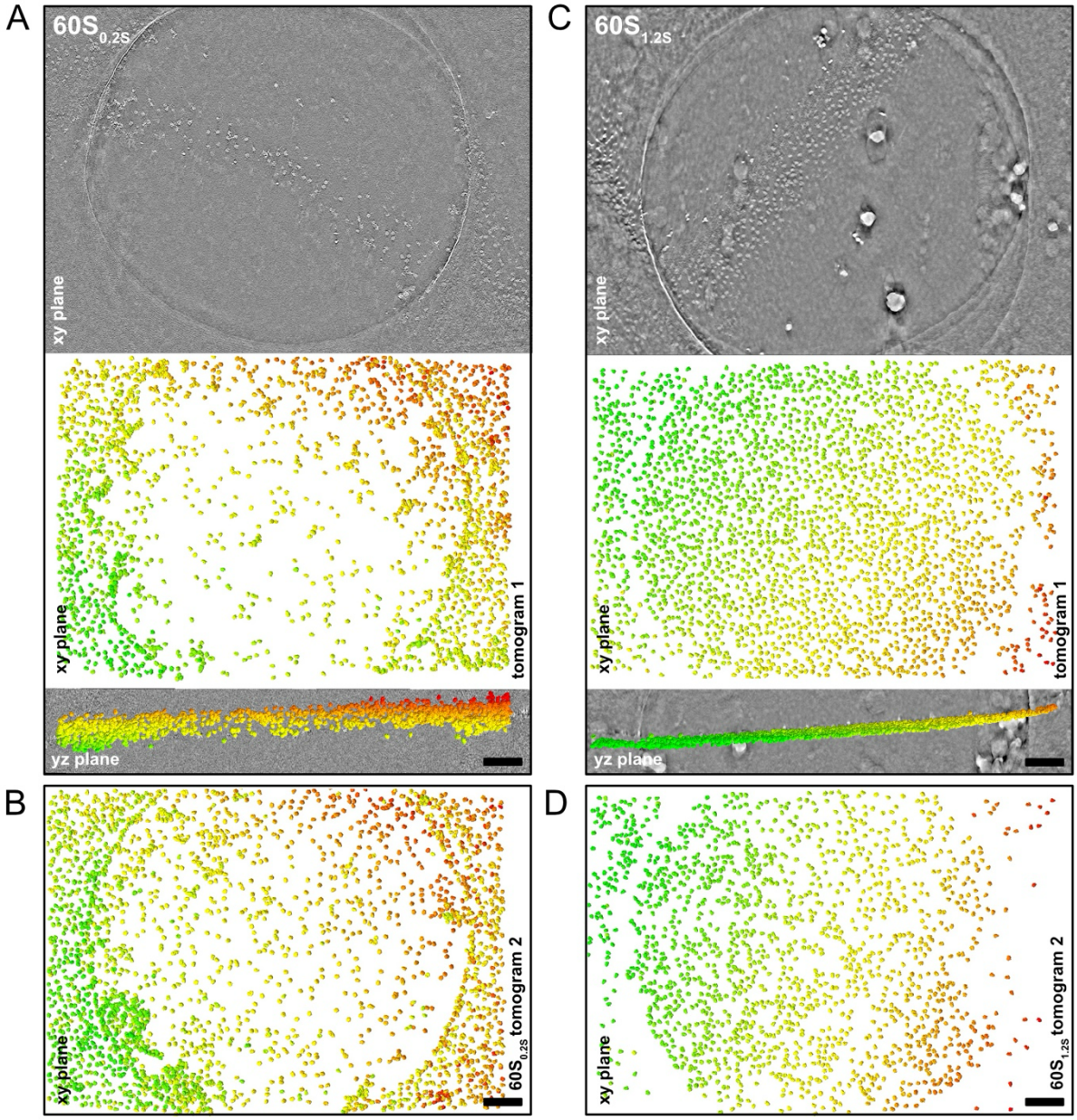

Supplementary Figure 5: 60S ribosomal subunit distribution in vitreous ice. Tomographic reconstruction of 60S ribosomal particles vitrified in the presence of 0.2% sucrose **(A,B)** and 1.2% sucrose **(C,D)**. The particle distribution above two representative carbon holes per condition is shown in xy plane **(A-D)**. Particle coordinates of cleaned subtomograms were mapped back into the tomograms using the ArtiaX plugin (5) in ChimeraX v1.7 (6) and coloured according to their position in the z-dimension (from green to red). In addition, for one tomogram per condition, the central slices through a deconvolved version of the tomogram in xy plane and yz plane are shown **(A,C)**. Scale bars represent 200 nm.

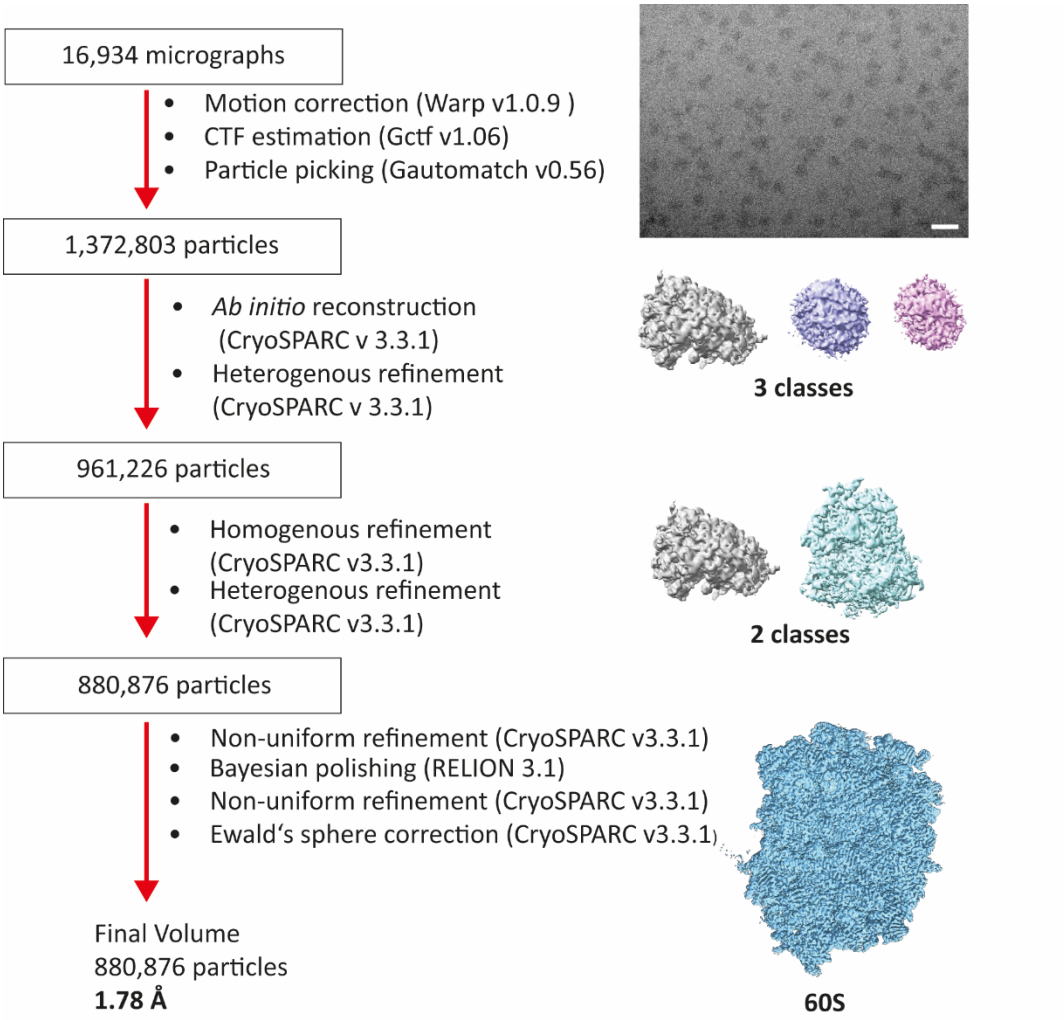

Supplementary Figure 6: Processing scheme for the single-particle reconstruction of the 60S ribosomal subunit. Initial motion correction was performed with Warp (3), followed by CTF estimation using Gctf (7) and particle picking in Gautomatch (8). A resulting representative micrograph is shown. Particle images were extracted in RELION 3.1 (9) and imported to CryoSPARC v3.3.1 (1). After *ab initio* reconstruction the particles were subjected to consecutive hetero- and homogenous refinement to remove non-ribosomal particles and 80S ribosomal particles (initial volumes used for hetero-refinement are shown). $60S_{1.2S}$ ribosomal subunit particles were further refined using non-uniform (NU) refinement (correcting for higher order aberrations) and CTF-per particle refinement. The refined particles were exported to RELION 3.1 for Bayesian polishing. Polished particles with a pixel size of 0.618 Å were re-imported to CryoSPARC for a final NU refinement and reconstruction with Ewald's sphere correction, which improved the global resolution of the density map to 1.78 Å ($FSC_{0.143}$). Scale bar in micrograph represents 50 nm.

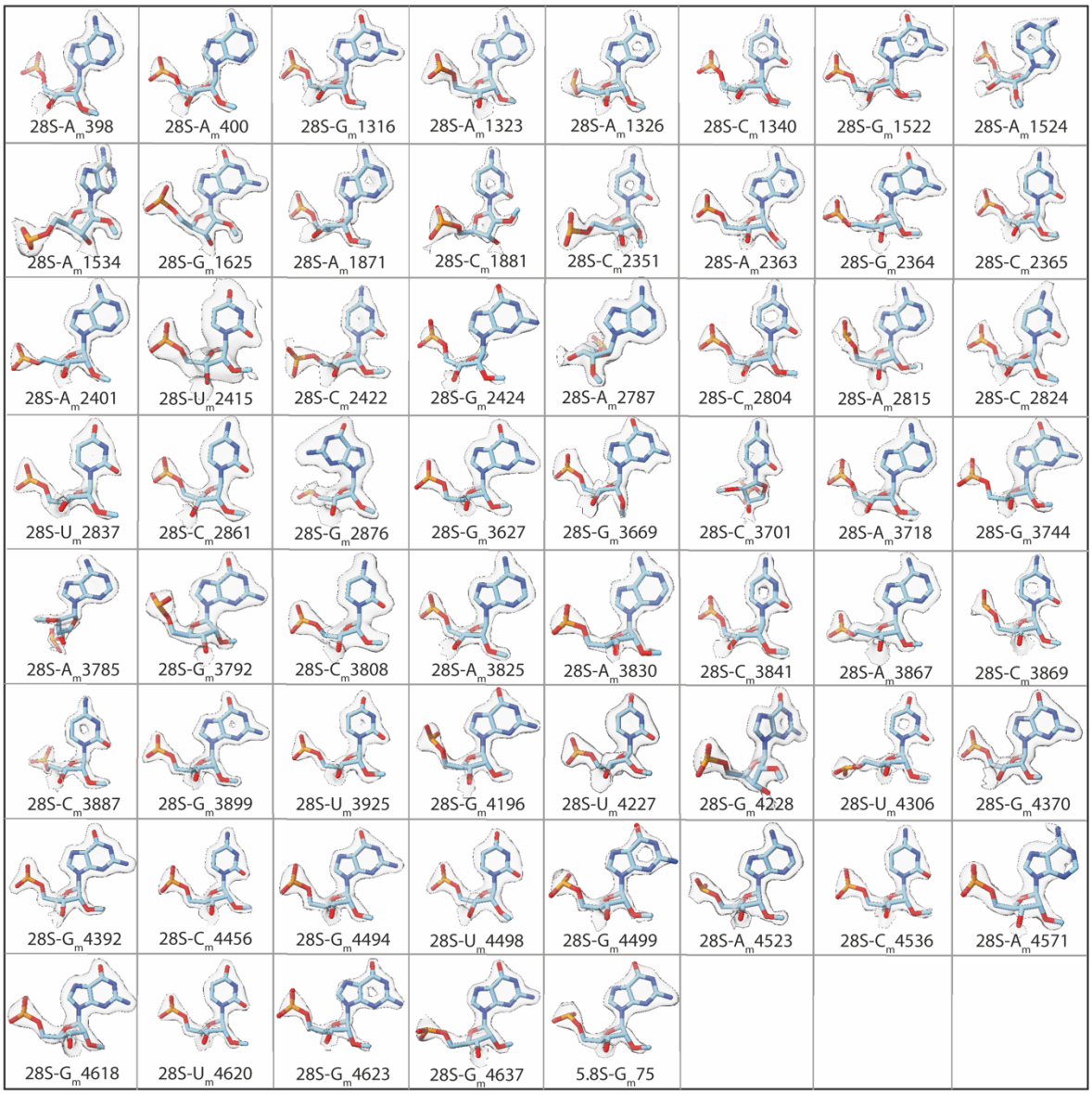

Supplementary Figure 7: Close-up views of O2'-methylated nucleotides in the 60S ribosomal subunit. Modified nucleotides are shown as sticks with transparent density adjusted to 5-14 σ-levels for similar visual impression.

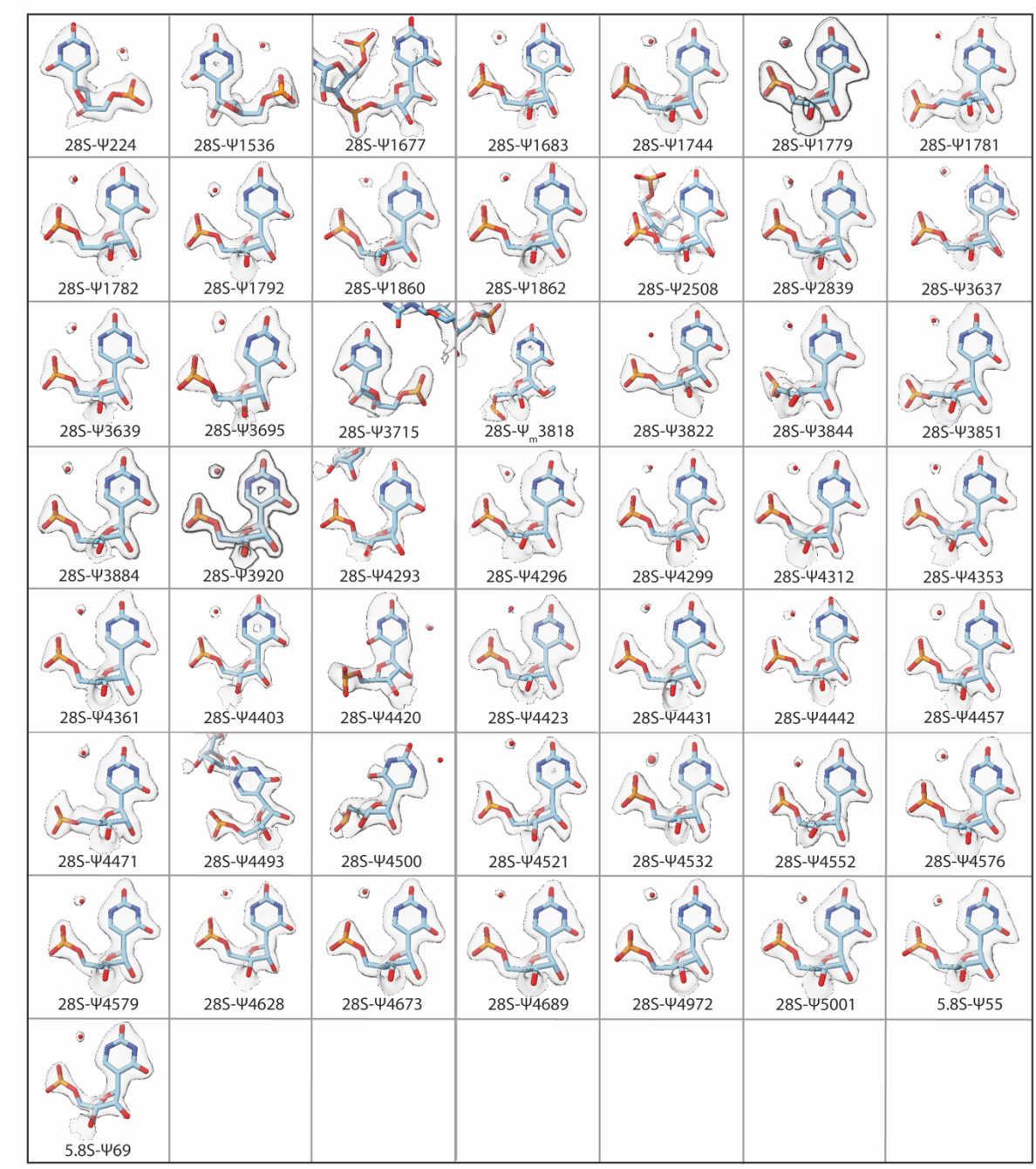

Supplementary Figure 8: Close-up views of identified pseudouridines and imide interaction partners in the 60S ribosomal subunit. Pseudouridines are shown as sticks, water molecules as red dots with surrounding transparent density adjusted to 5-14 σ-levels for similar visual impression.

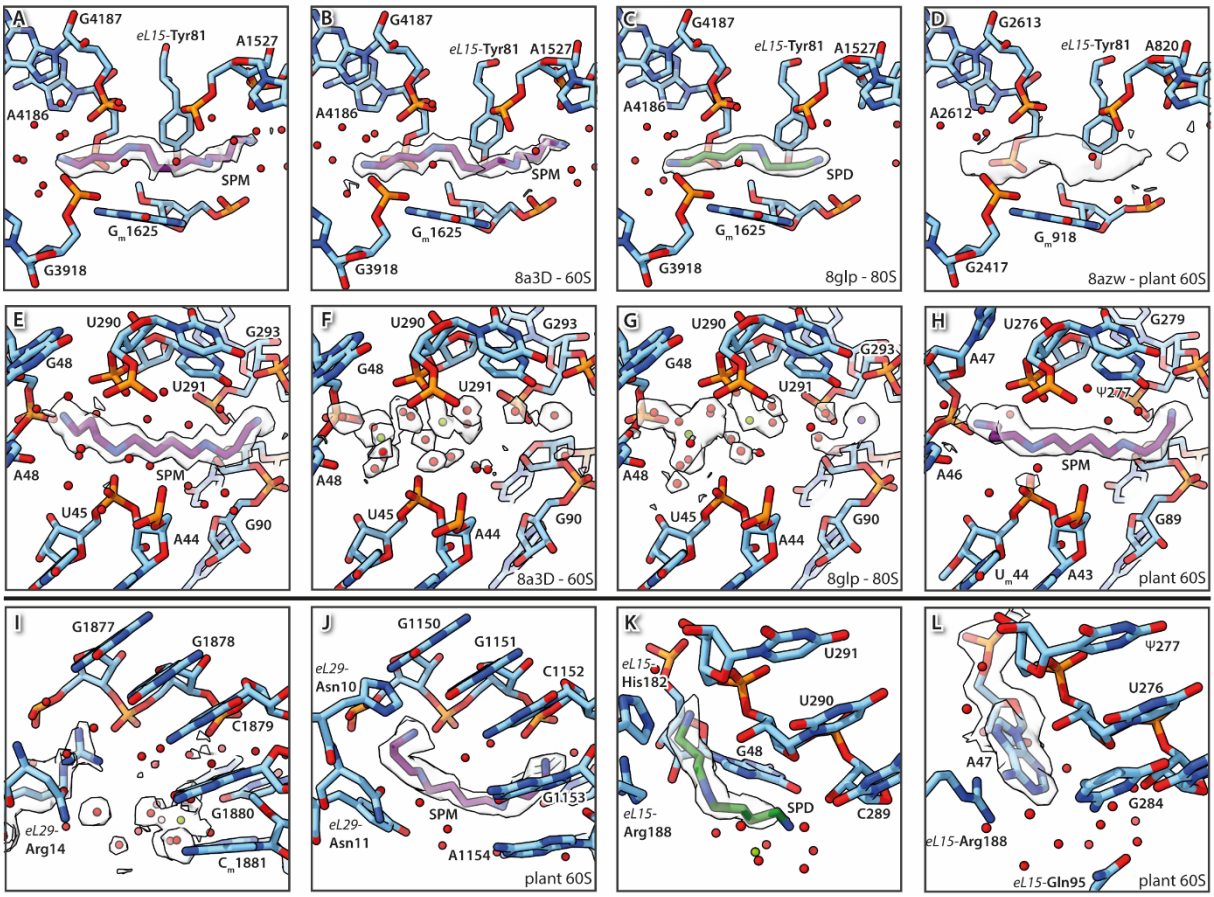

Supplementary Figure 9: Comparison of exemplary polyamines in high-resolution structures of 60S ribosomal subunits. **(A)** Spermine close to G_m1625 of 28S rRNA in 60S from HeLa cells (this work). **(B)** The same position in 60S from HEK cells with spermine bound [PDB-ID: 8A3D, (10)] and **(C)** 80S from HEK cells with spermidine bound [PDB-ID: 8QLP, (11)]. **(D)** No polyamine was built into the density found at the same position in 60S from tobacco plant [PDB-ID: 8AZW, (12)]. **(E)** Spermine was found close to nucleotide G46 of 28S rRNA in 60S from HeLa cells (this work). **(F, G)** The same position in 60S from HEK cells and 80S from HEK cells with water and Mg^{2+} binding there and **(H)** spermine binding instead in 60S from tobacco plant. **(I)** Mg^{2+} and water binding to 60S from HeLa cells (this work) at loop HS41 with el29-Arg14 closely associated. **(J)** In plant 60S spermine is binding there with el29-Asn10 close by. **(K)** Spermidine binding to H21 in the here presented structure and nucleotide G48 of 28S rRNA pointing away compared to **(L)** the plant 60S showing a different conformation of nucleotide A47 at this position and no polyamine binding. Nucleobases and peptides are shown as sticks, water molecules as red spheres and magnesium ions as green spheres. Transparent electron density at a contour level of 5.5 σ is shown.

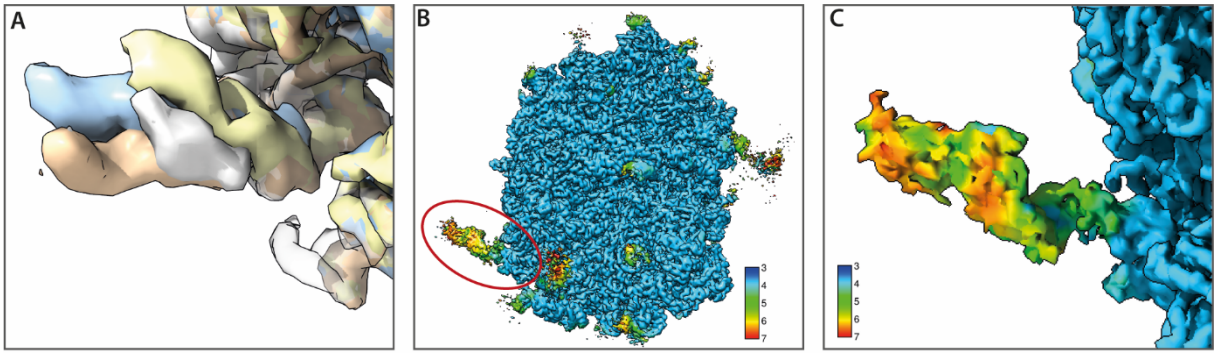

Supplementary Figure 10: Impressions from the 3D variability analysis for ES39. (A) Close-up views of four distinct states of expansion segment ES39, each comprising ~30k particles of the original 880k particle set are shown colored in light blue (state 1), peach (state 2), yellow (state 3) and white (state 4), respectively. State 4 also shows an enhanced density for parts of neighboring ES7 (B) Local resolution map for state 1 shows density for the previously "missing" structure at a magnitude below the rest of the map. (C) Close-up view of the state 1 in (B) shows clear helical conformation with the map being at 5-6 Å resolution.

Supplementary Table 1. Data collection and refinement statistics

Data Collection	8QYX EMD-18765
Magnification	105,000x
Voltage (kV)	300
Electron dose ($e^-/Å^2$)	49
Nominal defocus range (μm)	-0.5 to -2
Pixel size (Å/px)	0.412
Map sharpening B factor ($Å^2$)	38.3
Resolution (Å, 0.143 FSC)	1.78
Symmetry imposed	C1
Initial particle images (no.)	1,370,000
Final particle images (no.)	880,818
Final map pixel size (decimated, Å/px)	0.616
Model refinement	
Initial model used (PDB ID)	6EKO
Model resolution (Å) FSC threshold = 0.143	1.80
Model resolution (Å) FSC threshold = 0.5	1.86
Model vs. map correlation coefficient (cc_mask)	0.83
Model composition	
Non-hydrogen atoms	150,022
Protein residues	6,429
RNA residues	3,986
Water	11,854
Ligands	235
B factors ($Å^2$) (mean)	
Protein	17.78
RNA	26.34
Water	14.32
Ligands	13.04
Validation (proteins)	
Poor rotamers (%)	0.13
Ramachandran outliers (%)	0.03
Ramachandran favored (%)	98.40
Bad backbone bonds (%)	0.0
Bad backbone angles	0.0
Validation (nucleic acids)	
Correct sugar puckers (%)	78
Good backbone conformations (%)	83
Clash score, all atoms	4.75
Molprobity score	1.24

Supplementary Table 2. Data collection and processing statistics tilt series

Data Collection	**$60S_{0.2S}$**	**$60S_{1.2S}$**
Magnification	19,500x	19,500x
Voltage (kV)	300	300
Camera	K3	K3
Energy filter slit width (eV)	20	20
Objective aperture (µm)	100	100
Movie frames per tilt	10	10
Target dose rate on camera (e^-/px/s)	8.4	7.8
Electron dose tilt series ($e^-/Å^2$)	109	102
Tilt range (°)	±48 (dose symmetric)	±48 (dose symmetric)
Tilt increment (°)	3	3
Defocus range (µm)	-3 to -7	-3 to -7
Pixel size (Å)	2.2425	2.2425
Data processing		
Symmetry imposed	C1	C1
Subtomograms extracted (no.)	210,000	124,000
Subtomograms final (no.)	192,277	54,574
Subtomogram voxel size (Å)	8.97	8.97

Supplementary Table 3. Relative ice thickness of representative tomograms

Tomograms 60S 0.2% sucrose	Thickness (nm)			Mean value (nm)	Deviation (nm)
MGS001_T2_ts_001.mrc	60	62	65	62.3	2.5
MGS001_T2_ts_002.mrc	58	57	60	58.3	1.5
MGS001_T2_ts_003.mrc	46	48	49	47.7	1.5
MGS001_T2_ts_004.mrc	47	48	47	47.3	0.6
MGS001_T2_ts_005.mrc	50	51	52	51.0	1.0
MGS001_T2_ts_006.mrc	50	51	52	51.0	1.0
MGS001_T2_ts_007.mrc	50	52	49	50.3	1.5
MGS001_T2_ts_008.mrc	44	45	52	47.0	4.4
MGS001_T2_ts_009.mrc	47	74	51	57.3	14.6
MGS001_T2_ts_010.mrc	45	50	45	46.7	2.9
MGS001_T3_ts_002.mrc	48	50	55	51.0	3.6
MGS001_T3_ts_003.mrc	48	43	122	71.0	44.2
				53.4	6.6
Tomograms 60S 1.2% sucrose	**Thickness (nm)**			**Mean value (nm)**	**Deviation (nm)**
MGS001_T1_ts_001.mrc	48	50	47	48.3	1.5
MGS001_T1_ts_002.mrc	48	37	45	43.3	5.7
MGS001_T1_ts_003.mrc	53	51	49	51.0	2.0
MGS001_T1_ts_004.mrc	51	51	56	52.7	2.9
MGS001_T1_ts_005.mrc	43	46	53	47.3	5.1
MGS001_T1_ts_006.mrc	45	56	49	50.0	5.6
MGS001_T1_ts_007.mrc	44	46	49	46.3	2.5
MGS001_T1_ts_008.mrc	53	52	50	51.7	1.5
MGS001_T1_ts_009.mrc	52	50	53	51.7	1.5
MGS001_T1_ts_010.mrc	50	53	50	51.0	1.7
MGS001_T1_ts_011.mrc	50	44	48	47.3	3.1
MGS001_T1_ts_012.mrc	48	52	52	50.7	2.3
				49.3	3.0

Supplementary Table 4: Overview of *in silico* 3D variability and sorting results of selected variable regions

Structural element	Description of computationally isolated states
L-Stalk	improved density in three different orientations with 140k particles, 231k particles and 235k particles, local resolution >6 Å
ES7	very heterogenous and seemingly only partially ordered at best, no distinctive states found
ES27	isolated three helical states with 55k, 29k and 60k particles
P-Stalk	seems disordered, sorting led to no improvement
ES5	two different helical orientations, not well defined with 250k particles each
ES31	seems disordered, sorting led to no improvement
ES39	helical, with different orientations, sorting in distinct states (~30k particles) improved to 5 Å local resolution for a subset

Supplementary Table 5. Comparison of rRNA modifications

Chain	Position	This study	Taoka *et al.* (14)	Holm *et al.* (11)	Faille *et al.* (10)	Smirnova *et al.* (12)	Natchiar *et al.* (13)
Organism cell line		Human HeLa	Human HeLa	Human HEK Expi293F	Human HEK Expi293F	Tobacco plant	Human HeLa
28S	224	Ψ224					
28S	237						xp^{6}G237
28S	373						Gm373
28S	398	Am398	Am398	Am398	Am398		Am398
28S	400	Am400	Am400	Am400	Am400		
28S	729						m^{2}G729
28S	978						m^{2}G978
28S	1316	Gm1316	Gm1316	Gm1316	Gm1316		Gm1316
28S	1322	m1A1322	m1A1322	m1A1322	m1A1322	1mA656	m^{1}A1322
28S	1323	Am1323	Am1323				
28S	1326	Am1326	Am1326	Am1326	Am1326	Am660	Am1326
28S	1340	Cm1340	Cm1340	Cm1340	Cm1340	Cm674	
28S	1348						xp^{4}U1348
28S	1456						m^{3}C1456
28S	1517						m^{2}G1517
28S	1522	Gm1522	Gm1522	Gm1522	Gm1522	Gm815	Gm1522
28S	1524	Am1524	Am1524	Am1524	Am1524	Am817	Am1524
28S	1534	Am1534	Am1534	Am1534	Am1534	Am827	Am1534
28S	1536	Ψ1536	Ψ1536	Ψ1536	Ψ1536	Ψ829	
28S	1574						xp^{6}G1574
28S	1582		Ψ1582	Ψ1582	Ψ1582		Ψ1582
28S	1605						m^{7}G1605
28S	1625	Gm1625	Gm1625	Gm1625	Gm1625	Gm918	Gm1625
28S	1659						xp^{4}U1659
28S	1677	Ψ1677	Ψ1677	Ψ1677	Ψ1677	Ψ970	Ψ1677
28S	1683	Ψ1683	Ψ1683	Ψ1683	Ψ1683	Ψ976	Ψ1683
28S	1744	Ψ1744	Ψ1744	Ψ1744	Ψ1744	Ψ1016	
28S	1760	ND	Gm1760		ND		
28S	1773	ND	Um1773		ND		
28S	1779	Ψ1779	Ψ1779	Ψ1779	ND		
28S	1781	Ψ1781	Ψ1781	Ψ1781	Ψ1781		
28S	1782	Ψ1782	Ψ1782	Ψ1782	Ψ1782		
28S	1792	Ψ1792	Ψ1792	Ψ1792	Ψ1792	Ψ1064	
28S	1797						xe^{7}G1797
28S	1859	m4C					
28S	1860	Ψ1860	Ψ1860	Ψ1860	Ψ1860	Ψ1133	m^{1}Ψ1860
28S	1862	Ψ1862	Ψ1862	Ψ1862	Ψ1862	Ψ1135	
28S	1866						m^{3}U1866
28S	1871	Am1871	Am1871	Am1871	Am1871	Am1144	Am1871

28S	1881	Cm1881	Cm1881	Cm1881			
28S	1883						Gm1883
28S	1909						xp^{7}G1909
28S	2050						Gm2050
28S	2297						xe^{7}G2297
28S	2351	Cm2351	Cm2351	Cm2351	Cm2351	Cm1448	
28S	2363	Am2363	Am2363	Am2363	Am2363	Am1460	Am2363
28S	2364	Gm2364	Gm2364	Gm2364	Gm2364	Gm1461	Gm2364
28S	2365	Cm2365	Cm2365	Cm2365	Cm2365		Cm2365
28S	2380						m^{6}G2380
28S	2401	Am2401	Am2401	Am2401	Am2401		Am2401
28S	2415	Um2415	Um2415	Um2415	Um2415		
28S	2422	Cm2422	Cm2422	Cm2422	Cm2422		Cm2422
28S	2424	Gm2424	Gm2424	Gm2424	Gm2424		Gm2424
28S	2508	Ψ2508	Ψ2508	Ψ2508	Ψ2508		Ψ2508
28S	2522						m^{7}G2522
28S	2632	Ψ2632	Ψ2632	Ψ2632	Ψ2632		
28S	2754						xp^{6}G2754
28S	2773						Gm2773
28S	2786						xp^{3}Cm2786
28S	2787	Am2787	Am2787	Am2787	Am2787		
28S	2804	Cm2804	Cm2804	Cm2804	Cm2804	Cm1862	Cm2804
28S	2815	Am2815	Am2815	Am2815	Am2815		
28S	2824	Cm2824	Cm2824	Cm2824	Cm2824		
28S	2837	Um2837	Um2837	Um2837	Um2837	Um1894	
28S	2835	A	Ψ2835		A		
28S	2839	Ψ2839	Ψ2839	Ψ2839	Ψ2839		
28S	2861	Cm2861	Cm2861	Cm2861	Cm2861		Cm2861
28S	2876	Gm2876	Gm2876	Gm2876	Gm2876		
28S	3627	Gm3627	Gm3627	Gm3627	Gm3627	Gm2127	
28S	3637	Ψ3637	Ψ3637	Ψ3637	Ψ3637	Ψ2137	
28S	3639	Ψ3639	Ψ3639	Ψ3639	Ψ3639	Ψ2139	
28S	3669	Gm3669					
28S	3695	Ψ3695	Ψ3695	Ψ3695	Ψ3695	Ψ2194	
28S	3701	Cm3701	Cm3701	Cm3701	Cm3701	Cm2200	Cm3701
28S	3715	Ψ3715	Ψ3715	Ψ3715	Ψ3715	Ψ2214	Ψ3715
28S	3718	Am3718	Am3718	Am3718	Am3718		Am3718
28S	3723	ND	Am3723	Am3723	Am3723	Am2223	Am3723
28S	3724			Am3724			
28S	3729	ND	Ψ3729	Ψ3729	Ψ3729		Ψ3729
28S	3734	ND	Ψ3734	Ψ3734	ND		
28S	3744	Gm3744	Gm3744	Gm3744	Gm3744		
28S	3758	ND	Ψ3758	Ψ3758	ND	Ψ2257	
28S	3760	ND	Am3760	Am3760	ND	Am2259	
28S	3762	ND	Ψ3762	Ψ3762	ND	Ψ2261	m^{1}Ψ3762

28S	3764	ND	Ψ3764	Ψ3764	ND	Ψ2263	Ψ3764
28S	3768	ND	Ψ3768	Ψ3768	ND	Ψ2267	
28S	3770	ND	Ψ3770	Ψ3770	ND	Ψ2269	
28S	3782	m5C3782	m5C3782	m5C3782	m5C3782	m5C2281	m^5C3782
28S	3785	Am3785	Am3785	Am3785	Am3785	Am2284	Am3785
28S	3792	Gm3792	Gm3792	Gm3792	Gm3792	Gm2291	Gm3792
28S	3808	Cm3808	Cm3808	Cm3808	Cm3808		
28S	3818	Ψm3818	Ψm3818	Ψm3818	Ψm3818	Ψ2317	
28S	3822	Ψ3822	Ψ3822		ND	Ψ2321	
28S	3825	Am3825	Am3825	Am3825	Am3825	Am2324	Am3825
28S	3830	Am3830	Am3830	Am3830	Am3830	Am2329	
28S	3841	Cm3841	Cm3841	Cm3841	Cm3841	Cm2340	
28S	3844	Ψ3844	Ψ3844	Ψ3844	Ψ3844		
28S	3851	Ψ3851	Ψ3851	Ψ3851	Ψ3851	Um2350	
28S	3853		Ψ3853	Ψ3853	Ψ3853		
28S	3867	Am3867	Am3867	Am3867	Am3867		Am3867
28S	3869	Cm3869	Cm3869	Cm3869	Cm3869	Cm2368	Cm3869
28S	3880						xp^7G3880
28S	3884	Ψ3884	Ψ3884	Ψ3884	Ψ3884		
28S	3887	Cm3887	Cm3887	Cm3887	Cm3887		Cm3887
28S	3897						ac^7G3897
28S	3899	Gm3899	Gm3899	Gm3899	Gm3899	Gm2398	$ac^7Gm3899$
28S	3909						Cm3909
28S	3920	Ψ3920	Ψ3920	Ψ3920	Ψ3920	Ψ2419	
28S	3925	Um3925	Um3925	Um3925	Um3925	Um2424	
28S	3944	ND	Gm3944	Gm3944	ND		
28S	3959	ND	Ψ3959	ND	ND		
28S	4042	ND	Gm4042	ND	ND		
28S	4054	ND	Cm4054	ND	ND		
28S	4083						m^5U4083
28S	4129						m^6G4129
28S	4185						m^6G4185
28S	4194						xp^4U4194
28S	4196	Gm4196	Gm4196	Gm4196	Gm4196	Gm2622	Gm4196
28S	4220	m6A4220	m6A4220	m6A4220	m6A4220		m^6A4220
28S	4227	Um4227	Um4227	Um4227	Um4227	Ψm2653	
28S	4228	Gm4228	Gm4228	Gm4228	Gm4228	Gm2654	
28S	4293	Ψ4293	Ψ4293	Ψ4293	Ψ4293		Ψ4293
28S	4296	Ψ4296	Ψ4296	Ψ4296	Ψ4296		$m^1Ψ4296$
28S	4299	Ψ4299	Ψ4299	Ψ4299	Ψ4299		
28S	4306	Um4306	Um4306	Um4306	Um4306	Um2732	Um4306
28S	4312	Ψ4312	Ψ4312	Ψ4312	Ψ4312	Um2738	
28S	4335						m^5C4335
28S	4353	Ψ4353	Ψ4353	Ψ4353	Ψ4353		

28S	4355						xe^{6}G4355
28S	4361	Ψ4361	Ψ4361	Ψ4361	Ψ4361		
28S	4370	Gm4370	Gm4370	Gm4370	Gm4370	Gm2796	Gm4370
28S	4371						m^{2}xp^{7}G4371
28S	4392	Gm4392	Gm4392	Gm4392	Gm4392	Gm2818	
28S	4403	Ψ4403	Ψ4403	Ψ4403	Ψ4403	Ψ2829	Ψ4403
28S	4415						m^{1}A4415
28S	4420	Ψ4420	Ψ4420	Ψ4420	Ψ4420		
28S	4423	Ψ4423	Ψ4423	Ψ4423	Ψ4423		
28S	4431	Ψ4431	Ψ4431	Ψ4431	Ψ4431	Ψ2857	
28S	4442	Ψ4442	Ψ4442	Ψ4442	Ψ4442	Ψ2868	Ψ4442
28S	4447	m5C4447	m5C4447	m5C4447	m5C4447	m5C2873	m^{5}C4447
28S	4450						Ψ4450
28S	4456	Cm4456	Cm4456	Cm4456	Cm4456	Cm2882	
28S	4457	Ψ4457	Ψ4457	Ψ4457	Ψ4457	Ψ2883	
28S	4471	Ψ4471	Ψ4471	Ψ4471	Ψ4471	Ψ2897	
28S	4472						m^{6}G4472
28S	4483						m^{4}C4483
28S	4493	Ψ4493	Ψ4493	Ψ4493	Ψ4493		
28S	4494	Gm4494	Gm4494	Gm4494	Gm4494	Gm2920	Gm4494
28S	4498	Um4498	Um4498	Um4498	Um4498	Um2924	
28S	4499	Gm4499	Gm4499	Gm4499	Gm4499	Gm2925	
28S	4500	Ψ4500	Ψ4500	Ψ4500	Ψ4500	Ψ2926	Ψ4500
28S	4521	Ψ4521	Ψ4521	Ψ4521	Ψ4521	Ψ2947	
28S	4523	Am4523	Am4523	Am4523	Am4523	Am2949	Am4523
28S	4529						m^{6}G4529
28S	4530	m3U4530	m3U4530	m3U4530	m3U4530	m3U2956	m^{3}U4530
28S	4531			Ψ4531			Ψ4531
28S	4532	Ψ4532	Ψ4532	Ψ4532	Ψ4532	Ψ2958	
28S	4536	Cm4536	Cm4536	Cm4536	Cm4536	Cm2962	Cm4536
28S	4550						m^{7}G4550
28S	4552	Ψ4552	Ψ4552	Ψ4552	Ψ4552	Ψ2978	
28S	4564						m^{7}A4564
28S	4569			Ψ4569			
28S	4571	Am4571	Am4571	Am4571	Am4571		Am4571
28S	4576	Ψ4576	Ψ4576	Ψ4576	Ψ4576		
28S	4579	Ψ4579	Ψ4579	Ψ4579	Ψ4579		
28S	4590		Am4590	Am4590	Am4590		
28S	4597						m^{3}U4597
28S	4618	Gm4618	Gm4618	Gm4618	Gm4618		
28S	4620	Um4620	Um4620	Um4620	Um4620		Um4620
28S	4623	Gm4623	Gm4623	Gm4623	Gm4623		Gm4623
28S	4628	Ψ4628	Ψ4628	Ψ4628	Ψ4628		Ψ4628
28S	4636		Ψ4636	Ψ4636	ND		Ψ4636

28S	4637	Gm4637	Gm4637	Gm4637	Gm4637		Gm4637
28S	4671						m^4C4671
28S	4673	Ψ4673	Ψ4673	Ψ4673	Ψ4673		
28S	4689	Ψ4689	Ψ4689	Ψ4689	Ψ4689		
28S	4690						ac^7G4690
28S	4870						Gm4870
28S	4872						m^2G4872
28S	4972	Ψ4972	Ψ4972	Ψ4972	Ψ4972		
28S	5001	Ψ5001	Ψ5001	Ψ5001	Ψ5001		
28S	5010		Ψ5010	Ψ5010	Ψ5010		
5.8S	14		Um14	Um14			Um14
5.8S	55	Ψ55	Ψ55	Ψ55	Ψ55		
5.8S	69	Ψ69	Ψ69	Ψ69	Ψ69		
5.8S	75	Gm75	Gm75	Gm75	Gm75	Gm78	
uL2	His-216	ox-His			ox-His		
uL3	His-245	met-His			met-His	met-His	
uL15	His-39	ox-His			ox-His		
eL29	Lys-5				met-Lys		
eL40	Lys-98	met-Lys			trimet-Lys	met-Lys	met-Lys
eL42	Lys-53				met-Lys		

Supplementary Table 6. Identified pseudouridines and their N3-binding partners

Position*	binding partner*	distance (Å)
224	water	2.92
1536	water	2.83
1677	phosphate 1676	2.64
1683	water	2.83
1744	water	2.78
1779	water	3.01
1781	water	2.62
1782	water	2.92
1792	water	2.89
1860	water	2.59
1862	water	2.75
2508	phosphate 2507	2.69
2839	water	3.07
3637	water	2.7
3639	water	2.8
3695	water	2.64
3715	U3713	2.85
3818	phosphate	2.87
3822	water	3.07
3844	water	2.77
3851	water	2.92
3884	water	3.2
3920	water	2.69
4293	ribose 4329	2.83
4296	water	2.75
4299	water	2.93
4312	water	2.63
4353	water	2.83
4361	water	2.59
4403	water	2.59
4420	water	2.51
4423	water	2.68
4431	water	2.93
4442	water	2.86
4457	water	2.72
4471	water	2.76
4493	ribose 4512	3.06
4500	water	2.68
4521	water	2.98
4532	water	2.91
4552	water	2.64
4576	water	3.09
4579	water	2.65

4628	water	2.66
4673	water	2.79
4689	water	3.05
4972	water	2.79
5001	water	2.71
5S-55	water	2.76
5S-69	water	2.8

*if not otherwise indicated, position numbers refer to a nucleotide in 28S rRNA

Supplementary Table 7: Comparison of identified polyamines in high-resolution cryo-EM structures

Neighbouring nucleotide in human 28S rRNA	**This work**	**Faille *et al.*** (10)	**Holm et al.** (11)	**Smirnova *et al.*** (12)
Organism and cell line	Human HeLa	Human HEK Expi 293F	Human HEK Expi 293F	Tobacco plant
U1649	PUT	H2O	SPD	H2O
G4175	PUT	Mg+H2O	Mg+H2O	H2O
5.8S U80	PUT	K+H2O	K+H2O	H2O
G1680	PUT	Mg+H2O	Mg+H2O	H2O
G1532	PUT	K+H2O	Mg+H2O	H2O
G3875	PUT	H2O	H2O	H2O
G3918	PUT	K+H2O	Mg+H2O	H2O
C3882	H2O	H2O	PUT	H2O
A4203	-	H2O	PUT	H2O
A4192	H2O	H2O	PUT	H2O
G4400	H2O	H2O	PUT	H2O
U2070	H2O	H2O	PUT	H2O
C1306	SPD	H2O	SPD	H2O
U291	SPD	H2O	Mg+H2O	A47
A39	SPD	Mg+H2O	SPD	SPD
A328	SPD	H2O	SPD	H2O
C1666	SPD	K+H2O	PUT	H2O
G2808	SPD	H2O	SPD	Mg+H2O
U3884	SPD	H2O	Mg+H2O	H2O
G4425	H2O	H2O	SPD	H2O
G2862	H2O	H2O	SPD	H2O
U1470	H2O	H2O	SPD	H2O
G2297	H2O	H2O	SPD	H2O
U13	-	H2O	SPD	H2O
U432	H2O	H2O	SPD	H2O
U1528	SPM	SPM	SPD	water*
A47	SPM	Mg + H20	Mg + H20	SPM
A1736	SPM	Mg+H2O	PUT- shifted	water
G1586	SPM	Mg+H2O	PUT	water
C1607	SPM	Mg+H2O	SPD	water
	*eL*29 Arg 14	*eL*29 Arg 14	*eL*29 Arg 14	SPM

*Inspection of the density suggests the presence of a polyamine instead of water (see Suppl. Figure 9D)

References

1. Punjani,A., Rubinstein,J.L., Fleet,D.J. and Brubaker,M.A. (2017) CryoSPARC: Algorithms for rapid unsupervised cryo-EM structure determination. *Nat Methods*, **14**, 290–296.
2. Afonine,P. V., Grosse-Kunstleve,R.W., Echols,N., Headd,J.J., Moriarty,N.W., Mustyakimov,M., Terwilliger,T.C., Urzhumtsev,A., Zwart,P.H. and Adams,P.D. (2012) Towards automated crystallographic structure refinement with *phenix.refine*. *Acta Crystallogr D Biol Crystallogr*, **68**, 352–367.
3. Tegunov,D. and Cramer,P. (2019) Real-time cryo-electron microscopy data preprocessing with Warp. *Nature Methods 2019 16:11*, **16**, 1146–1152.
4. Kimanius,D., Dong,L., Sharov,G., Nakane,T. and Scheres,S.H.W. (2021) New tools for automated cryo-EM single-particle analysis in RELION-4.0. *Biochem J*, **478**, 4169–4185.
5. Ermel,U.H., Arghittu,S.M. and Frangakis,A.S. (2022) ArtiaX: An electron tomography toolbox for the interactive handling of sub-tomograms in UCSF ChimeraX. *Protein Sci*, **31**, e4472.
6. Pettersen,E.F., Goddard,T.D., Huang,C.C., Meng,E.C., Couch,G.S., Croll,T.I., Morris,J.H. and Ferrin,T.E. (2021) UCSF ChimeraX : Structure visualization for researchers, educators, and developers. *Protein Science*, **30**, 70–82.
7. Zhang,K. (2016) Gctf: Real-time CTF determination and correction. *J Struct Biol*, **193**, 1–12.
8. Zhang,K. (2020) Gautomatch.
9. Scheres,S.H.W. (2012) RELION: Implementation of a Bayesian approach to cryo-EM structure determination. *J Struct Biol*, **180**, 519–530.
10. Faille,A., Warren,A.J. and Dent,K.C. (2023) The chemical landscape of the human ribosome at 1.67 Å resolution. bioRxiv doi: https://doi.org/10.1101/2023.02.28.530191, 28 February 2023, pre-print: not peer-reviewed.
11. Holm,M., Natchiar,S.K., Rundlet,E.J., Myasnikov,A.G., Watson,Z.L., Altman,R.B., Wang,H.Y., Taunton,J. and Blanchard,S.C. (2023) mRNA decoding in human is kinetically and structurally distinct from bacteria. *Nature*, **617**, 200–207.
12. Smirnova,J., Loerke,J., Kleinau,G., Schmidt,A., Bürger,J., Meyer,E.H., Mielke,T., Scheerer,P., Bock,R., Spahn,C.M.T., *et al.* (2023) Structure of the actively translating plant 80S ribosome at 2.2 Å resolution. *Nat Plants*, **9**, 987–1000.
13. Natchiar,S.K., Myasnikov,A.G., Kratzat,H., Hazemann,I. and Klaholz,B.P. (2017) Visualization of chemical modifications in the human 80S ribosome structure. *Nature*, **551**, 472–477.
14. Taoka,M., Nobe,Y., Yamaki,Y., Sato,K., Ishikawa,H., Izumikawa,K., Yamauchi,Y., Hirota,K., Nakayama,H., Takahashi,N., *et al.* (2018) Landscape of the complete RNA chemical modifications in the human 80S ribosome. *Nucleic Acids Res*, **46**, 9289–9298.